DOI: 10.13009/EUCASS2023-308
Aerospace Europe Conference 2023 – 10TH EUCASS – 9TH CEAS

Effect of aeroelasticity on the acoustic signature of TOP contoured rocket nozzles in overexpanded conditions

Martina Formidabile[⋆], *Woutijn J. Baars*[⋆†] *and Ferry F. J. Schrijer*[⋆]
[⋆]*Faculty of Aerospace Engineering, Delft University of Technology, 2629HS, The Netherlands*
martina.formidabile@gmail.com · W.J.Baars@tudelft.nl · F.F.J.Schrijer@tudelft.nl
[†]Corresponding author

Abstract

The focus of the present study is on the vibroacoustic loads that form during the startup of TOP contoured rocket nozzles. A urethane-based compliant walled nozzle is employed to investigate the effects of fluid-structure interactions on supersonic jet noise emission. Measurements of the nozzle-wall deformation, by means of tracking tracers on the nozzle lip, are synchronised with pressure-field microphones located in the near vicinity of the nozzle jet plume. Results are compared with those obtained from a baseline rigid wall nozzle fabricated from aluminium. Findings reveal that the inclusion of aeroelasticity in the experimental framework of sub-scale nozzle flow testing reduces the acoustic intensity over a large range of nozzle pressure ratios. Particularly, the aeroelasticity is responsible for the suppression of broadband shock noise and a strong tonal coupling just prior to FSS to RSS transition.

1. Introduction

Thrust optimised parabolic (TOP) contoured nozzles are commonly employed in rocket propulsion systems as they feature an excellent thrust-to-weight ratio, making their design versatile enough to be operated under a broad range of altitudes [1]. Typically, they present large area-ratios, in order to allow the combustion products to expand to low exit pressures, thus providing high exhaust velocities. During the startup and shutdown transients of liquid rocket engines, however, due to the turbopump system still accelerating to achieve the required pressure head, the combustion chamber is ramping from ambient to the nominal operating pressure defined by the design nozzle pressure ratio (NPR). When in overexpanded conditions the internal nozzle flow transitions from a Free Shock Separation (FSS) state to a Restricted Shock Separation (RSS) state, before reaching full flowing conditions during which the nozzle's internal flow topology remains unaltered [2]. Events of flow transition have been documented to produce intense side loads due to asymmetric flow separation and FSS → RSS transition [3]. In some occasions, off-axis forces have also caused catastrophic consequences: some notable examples are, for instance, that of the J-2S engine which was torn from its gimbal structure [4], or that of the Space Shuttle main engine (SSME) for which fatigue cracks and rupturing of the nozzle's coolant feed lines were identified.
Apart from the structural loads induced by the internal nozzle flow, also violent vibroacoustic loads (VAL) are produced during the ignition transient as a result of the unsteady flow in the exhaust plume [5]. Rocket plumes feature a number of noise generation mechanisms that are typical of non-ideally expanded supersonic jets, and comprise turbulent mixing noise [6, 7], broadband shock noise (BBSN) [8, 9] and resonant tones, like transonic resonance [10] and screech [11]. While some require full flowing conditions to be initiated, like screech, others can also occur during FSS, and are known to produce elevated acoustic levels that can be a threat to the surrounding environment and the payload of the launcher [12, 13, 14]. For over 50 years, the work of Eldred published in the NASA SP-8072 report [15], has represented the foundation for the prediction of launch vehicles acoustics. Even though, more recently, newer prediction methodologies have been compiled [16, 17, 18], a number of limitations still continue to exist and are typically associated with the fact that they assume full-flowing or adapted flow conditions. As such, the branch of research related to predicting transient ignition noise still heavily relies on experimental testing[19, 20, 21]. Yet, where laboratory-scale studies are concerned, they bring about a number of limitations in the results that they provide, attributable to the use of rigid wall nozzles, in which structural vibrations are suppressed. This was highlighted by Rojo et al. [20], who have evidenced significant differences in the data obtained from full-scale tests performed on the launch pad, which employ thin-walled nozzles that can vibrate, and from lab-scales ones, in which fluid-structure interactions are dampened. A preliminary effort in this direction was carried out by Tinney et al. [22]: they have characterised noise emission from a number of flexible nozzles having different degree of compliance and compared the results with those of a baseline stiff nozzle. Although

DOI: 10.13009/EUCASS2023-308

gross discrepancies were confirmed, the experimental investigation was performed by employing a single microphone, whose acquisition was decoupled from that of the nozzle lip movement. Within this framework, there still exists a large gap in the understanding of the acoustic signature produced by compliant TOP nozzles in a laboratory environment where the internal flow, the nozzle wall vibrations and the acoustic emission can be simultaneously monitored.
The aim of the current study is twofold: first, it summarises the efforts that have been undertaken to build a suitable nozzle testing facility within the laboratory of the Department of Flow Physics & Technology at the Delft University of Technology for the measurement of fluid-structure interaction phenomena during overexpanded operations of sub-scale TOP contoured nozzles. Next, it focuses on a mapping of the near and far-field acoustics (at both steep and shallow angle observer positions) of a compliant walled nozzle, while measuring its lip deformation. Tests under similar operating conditions are also performed on a baseline rigid walled nozzle featuring the same contour, in order to properly observe possible differences in the acoustic imprint of the two specimens, thereby quantifying the effects of aeroelasticity.

2. Experimental apparatus and procedure

2.1 ASCENT test facility and experimental conditions

Experimental activities were conducted employing the ASCENT nozzle test rig. Figure 1 presents a cut view of the rig, which allows for cold flow testing of reduced-scale nozzles. The working fluid is dry unheated air (T_o = 288 K), which is drawn from an external pressure vessel with a storage capacity of 300 m^3. When fully charged, the reservoir can contain approximately 484 kg of air, corresponding to a maximum theoretical stagnation pressure of 40 bar. Considering pressure losses through the feed system between external tank and settling chamber, and assuming atmospheric back pressure, in practice the maximum attainable NPR is around 32. Given the large volume of the pressure vessel, for tests lasting in the order of tens of seconds, the tank pressure can be considered constant and no active flow control is required. Total temperature and NPR are monitored employing, respectively, an IFM TM4431 Pt100 temperature sensor and an IFM PT5402 pressure transducer, which are directly inserted into the settling chamber, whereas a purposely written LabView algorithm allows for their recording at an acquisition frequency f_s of 2 kHz.

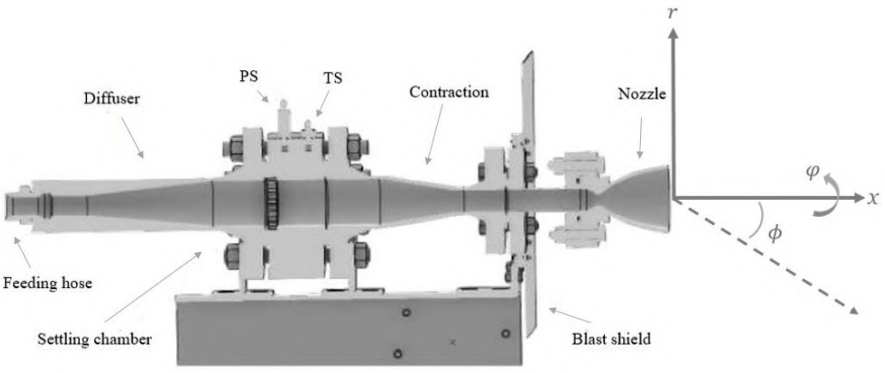

Figure 1: Academic Setup for unConventional Exhaust Nozzle Testing (ASCENT) test rig - Cut view of fluid components. Coordinate system defines x: axial direction, r: radial direction, φ: azimuthal angle, ϕ: polar angle (Adapted from De Kievit [23])

The rig is operated using a hand-regulated flow control valve: the NPR is manually adjusted, and the maximum achieved ramp rate for the current testing activities is around 7.5 s^{-1}, as shown in Figure 2. This is 3 orders of magnitude slower than a typical ramp of a full-scale liquid propellant rocket engine [20], meaning that the tests should be regarded as the ones associated with *quasi-steady* conditions.

2.2 Test articles

Experimental investigations have been performed using two axisymmetric TOP contoured nozzles, both employing the PAR3 contour based on the design by Ruf et al. [24], in order to simulate the separated flow behaviour typically observed during the ignition transient of rocket engines. Both nozzles present identical geometrical features, whereas they differ in their material properties and wall thickness (see Table 1). The wall coordinates and the resulting contour

DOI: 10.13009/EUCASS2023-308

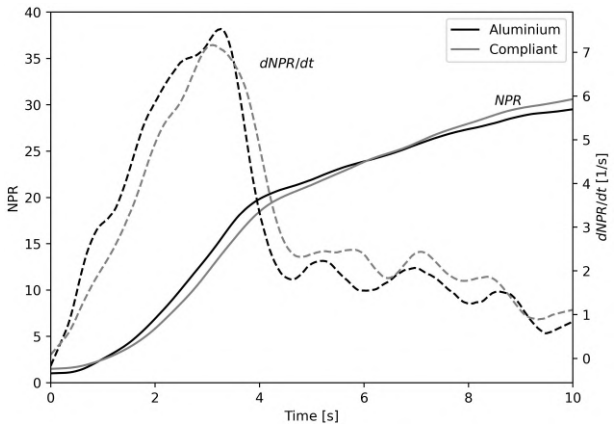

Figure 2: Sample recording of nozzle pressure ratio and ramp rate during two different startup tests

and wall pressure profile, as obtained from TDK [25], are illustrated in Figure 3: the exit-to-throat ratio ϵ of 30.29 requires a NPR of 699.8 to produce an ideally expanded flow at a design Mach number of 4.2.

Table 1: Geometric and material properties of the TOP nozzles

Property	**Symbol**	**Value**	**Unit**
Throat radius	r^*	8.175	mm
Throat expansion angle	θ^*	40	°
Exit radius	r_e	44.99	mm
Axial length	l	102.2	mm
Expansion ratio	ϵ	30.29	-
Nozzle	**Wall thickness** [mm]	**Material**	**Density** $[kg/m^3]$
Stiff	5	ALU 6082-T6	2700
Compliant	2	Polyurethane 66D	1102

The expansion angle at the throat for the nozzles used in the present study is chosen slightly higher than typical TOP contoured nozzles, to ensure that FSS to RSS transition occurs within the available NPR range. A previous study by Tinney et al. [22] who employ a nozzle with $r^* = 6.35$ mm and $\epsilon = 30.29$, has shown that transition occurs around NPR = 22. Based on this comparison, a throat radius for the current design of $r^* = 8.175$ mm, which stems from design constraints of the testing rig, is deemed acceptable.

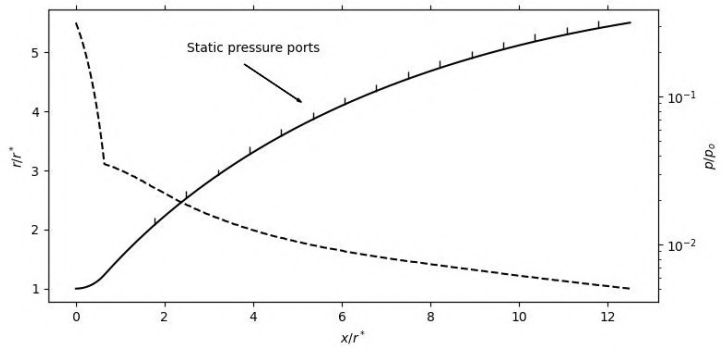

Figure 3: TOP contour profile (solid line) and corresponding wall pressure profile (dashed line), as obtained from TDK [25]

To confirm the hypothesis of flow transition in the NPR range of 22 to 25, a mapping of the wall pressure profile during a startup run was carried out. Given the rigidity of its design, the aluminium nozzle was equipped with a total of 3 axial arrays of static pressure ports, spaced of 90°, and situated at azimuthal angles $\varphi = 0°$, $\varphi = 90°$ and $\varphi = -90°$.

DOI: 10.13009/EUCASS2023-308

Each array consists of 15 ports along the axial direction, with a constant axial spacing of $\Delta x/r^* = 0.715$. The ports are spanned between $x/r^* = 1.768$ and 11.785 and are connected to a ScaniValve DSA3217 pressure scanner, which samples the static wall pressure at 500 Hz.

Static wall pressure distributions for a startup ramp up to NPR = 30 are presented in Figure 4 and already provide an understanding of the appearance and location of a number of flow features with increasing NPR. More specifically, as far as FSS → RSS is concerned, the transition point at all azimuthal stations is observed around NPR = 24.75, which lies in the expected range. Two pressure peaks are also visible in the RSS regime, with a maximum p/p_a of 1.4, and an approximate progression rate of dx/dNPR ≈ 4.15 mm/NPR. Although no such data is available for the flexible nozzle, Tinney et al. [22] have found that with increasing wall compliance flow transition occurs earlier, namely, at a lower NPR. This observation is also confirmed by others [26, 27] so that transition of the flexible nozzle is expected for NPR < 24.5.

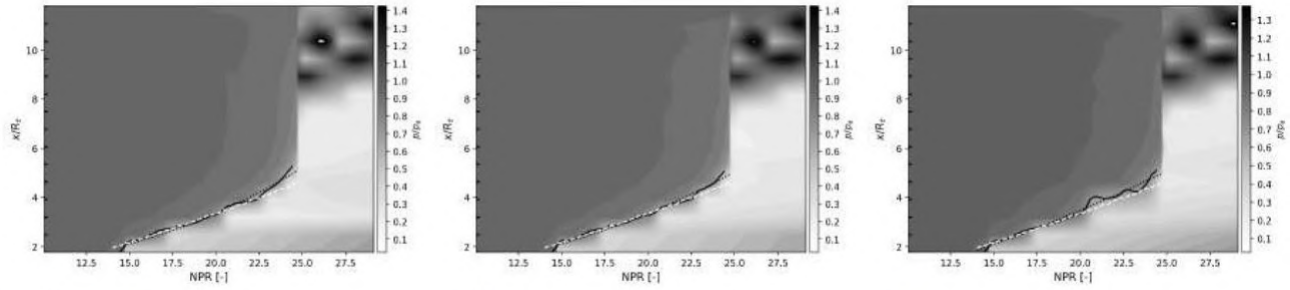

(a) $\frac{d(\text{NPR})}{dt} > 0$, $\varphi = 0°$ (b) $\frac{d(\text{NPR})}{dt} > 0$, $\varphi = 90°$ (c) $\frac{d(\text{NPR})}{dt} > 0$, $\varphi = -90°$

Figure 4: Wall pressure contours for a startup ramp case. The solid black line shows the separation point according to free interaction theory [28, 29] and the dashed white line shows the separation point according to the Stark criterion [30]

As for the compliant nozzle, it was fabricated in-house as a single piece from urethane-based elastomeric off-the-shelf components. To secure the nozzle onto the plenum face of the testing rig, while also providing reinforcement along the high pressure regions of the flow, the cast was surrounded with an aluminium two-piece outer shell up to an area ratio $A/A^* \approx 5$ downstream of the throat, which corresponds to 17% of the nozzle axial length.

Due to difficulties in modeling the nonlinear stress-strain behaviour of elastomeric materials, ground vibration testing (GVT) was performed on the compliant nozzle to characterise its dynamic behaviour. Modal testing consisted in equipping the internal lip of the nozzle with 8 equally spaced IPC accelerometers, whereas the excitation force, applied at a single excitation point, was provided using a Maul-Theet vImpact-61 automatic modal hammer. Findings are summarised in Table 2 and are going to be further discussed in subsection 3.1.

Table 2: Compliant nozzle fundamental and higher harmonics of the structural deformation modes

Oscillation mode[a]	**Resonant frequency [Hz]**	**Damping [%]**
Breathing	1559.14	3.60
Pure bending	277.15	3.85
Ovalisation	156.38	2.17
Triangular	325.87	2.63
Square	538.60	3.13

[a] Refer to Figure 8 for the azimuthal mode shapes of the nozzle lip

2.3 Experimental arrangement

In order to quantify the deformation of the compliant nozzle, when subjected to the high loads occurring during FSS and RSS flow states, a non-intrusive, full-field optical technique, similar to Particle Tracking Velocimetry (PTV), was employed, which consisted in performing structural measurements by imaging and tracking reflective fiducial markers distributed along the perimeter of the nozzle lip. As shown in Figure 5, the compliant nozzle was first spray-painted

DOI: 10.13009/EUCASS2023-308

with a matte black color to minimise reflections. Next, 24 equally spaced, highly reflective white circular dots, with an approximate diameter of $\varnothing 1.5 \pm 0.5$ mm, were manually painted on the surface.

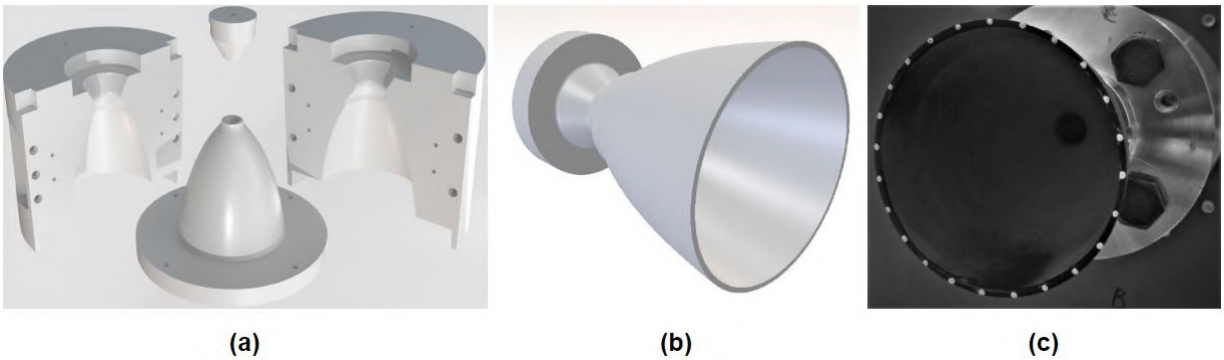

Figure 5: **a**) Exploded view of the mould assembly **b**) Compliant nozzle design rendering **c**) Detail of fiducial markers on compliant nozzle lip surface

Two Photron FASTCAM SA1.1 were employed to allow for stereoscopic reconstruction of the nozzle lip displacement. The cameras were operated in single-pulse mode, for a maximum of 10 seconds at an acquisition frequency of 2000 Hz. The Photrons communicate with a LaVision Programmable Timing Unit (PTU-X) for precise and syncronised trigger pulses, whereas acquisition was controlled by an acquisition computer, equipped with a high speed card, featuring a dual processor (Intel(R) Xeon(R) CPU E5-2630 v3 2.40 GHz each with 10 physical cores and 20 threads) and 64 GB of RAM, and running DaVis 10.2.1. This latter software was also employed for post-processing purposes: having performed a perspective calibration on the basis of a Type 10 calibration target, it was possible to analyse the nozzle wall dynamics using the IPR algorithm [31] to reconstruct the markers field (r, φ, x) in time.

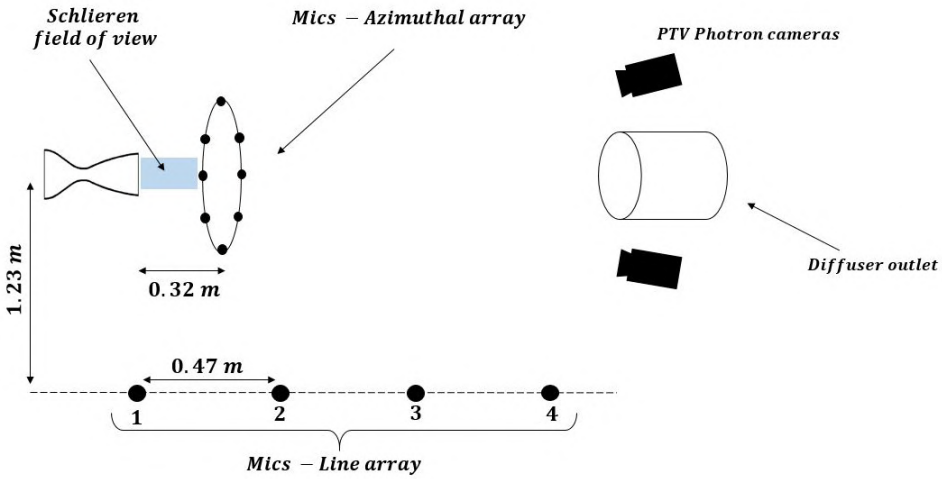

Figure 6: Plan view of the test setup

Acoustic sensing of the plume was simultaneously carried out in a non-acoustically treated environment. A number of IEPE-powered GRAS 46BE 1/4" CCP Free-field microphones were employed. Specific details of this model include a 3.6 mV/Pa nominal sensitivity, a frequency response range between 4 Hz and 100 kHz (±3 dB error) and a dynamic range up to 160 dB (ref: 20μPa). An acquisition frequency of 51.2 kHz was selected for all test runs and two different microphone configurations were chosen. An initial test campaign was carried out with 4 microphones, located on a line parallel to the jet axis at a radial distance of $r = 1.23$ m, with the microphones' diaphragm placed at grazing incidence to the jet axis. Having chosen to place the origin of the coordinate system at the nozzle exit plane, the streamwise (x) positions of the microphones relative to this origin are: $x = [0, 0.47, 0.94, 1.41]$ m. This corresponds to polar angles relative to the jet axis and nozzle exit plane of $\phi = [90, 69, 52.6, 41.1]$ deg. This placement is able to cover both shallow and steep angle observer locations, thereby offering useful insights into noise directionality.
A second investigation was carried out employing a circular array of 8 equally spaced microphones ($\varphi = 45°$) placed concentrically to the nozzle jet axis, as illustrated in Figure 7. The array was placed in the cone of maximum noise

DOI: 10.13009/EUCASS2023-308

intensity, at a radial distance from the nozzle centerline of $r = 23.5$ cm, and at an axial distance to the nozzle's exit plane of $d = 32$ cm, corresponding, for all microphones, to a fixed polar angle of $\phi \approx 36°$ with respect to the nozzle centerline.

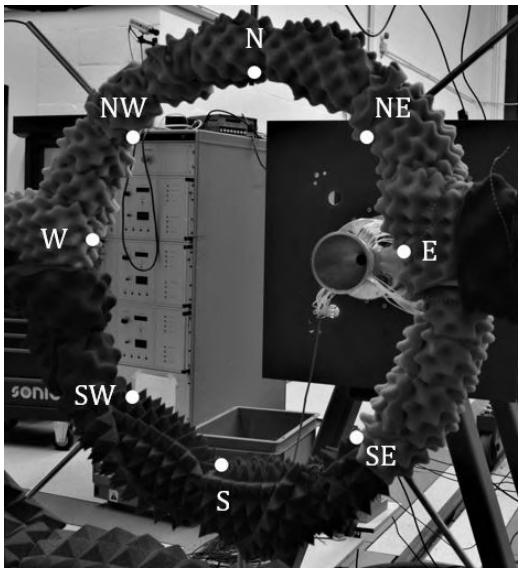

Figure 7: Circular array of microphones, with compass naming convention - White dots indicate microphone positions

Finally, for flow visualisation, a Z-configuration schlieren setup was built. A single Photron FASTCAM SA1.1 was placed in front of the lens system such that a pixel to millimiter ratio of approximately 4.5 mm^{-1} was achieved. 10 seconds of uninterrupted data were acquired at a frame rate of 500 Hz with an exposure time of 12 μs using Photron FastCam Viewer 4.0.

3. Results

3.1 Fourier-azimuthal decomposition of the nozzle lip deformation

Given the azimuthal spatial configuration of the fluctuating nozzle lip tracers, the signal was analysed in terms of its Fourier-azimuthal mode coefficients, which quantify the amplitude of the physical modes. Any signal that has an angular dependency can be Fourier transformed in azimuth to obtain time-dependent complex Fourier coefficients:

$$x(m,t) = \mathbb{F}_{\varphi}[x(\varphi,t)] \tag{1}$$

with m being the mode number. Depending on the discretisation of the grid, mode coefficients run from the negative to the positive azimuthal Nyquist wave number, in the following order: $m = [0, 1, 2, 3, ..., k_n, -k_n, ..., -3, -2, -1]$, with $k_n = N/2$, with N being the number of discretised azimuthal points.

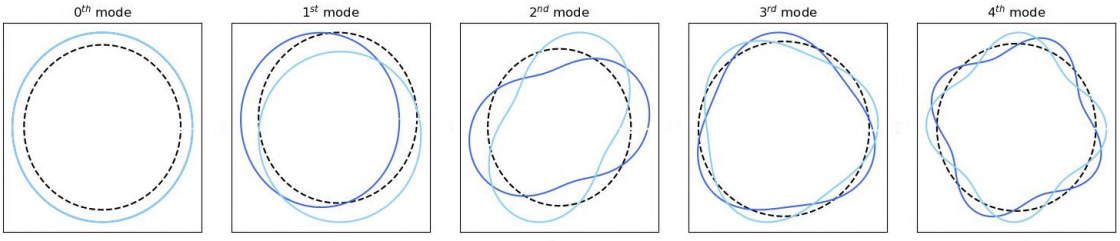

Figure 8: Fundamental and higher harmonics of the bending mode: 0^{th} = breathing mode, 1^{st} = pure bending, 2^{nd} = ovalization, 3^{rd} = traingular mode, 4^{th} = square mode. Dashed line correspond to the undeformed state; dark blue lines represent the positive modes; light blue lines represent the negative modes

DOI: 10.13009/EUCASS2023-308

Except for $m = 0$, positive and negative mode coefficients of the same order form conjugate pairs, that is $x(m,t) = x^*(-m,t)$. This means that, even though they represent the same mode shape, their phase in Cartesian space is offset by a quarter wavenumber (see Figure 8). Each mode coefficient can be regarded as the the m^{th} contribution to the original unsteady signal, and their magnitude gives an indication of how *active* one mode is within the signal. With a_n and b_n being, respectively, the positive and negative mode coefficients, a key parameter for the analysis of azimuth-dependent data is the time-dependent modal activity ρ:

$$\rho = \sqrt{a_n^2 + b_n^2} \tag{2}$$

The time-series of the first 5 modes are presented in Figure 9 for a (slow) transient increase in NPR. In terms of the modal activity, the ovalisation mode dominates with an increased activity around NPR = 22.3.

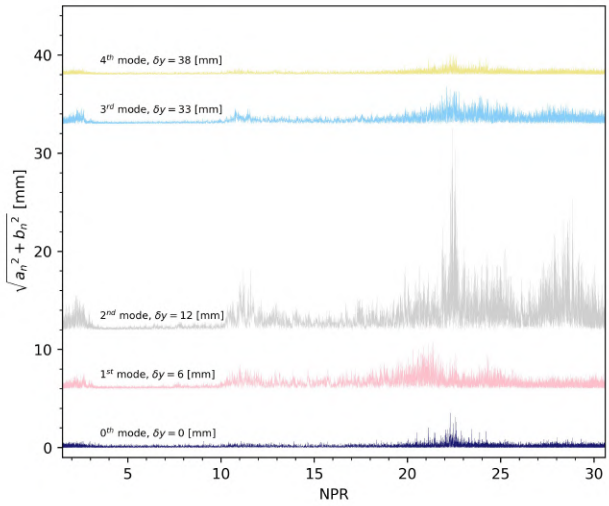

Figure 9: Nozzle-lip displacement intensity during a startup run: azimuthal mode activity of the fiducial markers fluctuation. Each time series is vertically offset by a value of δy indicated in the labels

Although at an order of magnitude lower, also the harmonics intensify their activity around the same NPR, lending support to the hypothesis of a forthcoming transition, which is moved forward with respect to the rigid nozzle case (recall transition in the rigid nozzle occurred at NPR = 24.7). Furthermore, the pure bending mode experiences its maximum activity slightly earlier, which suggests either the inception of an heightened shock foot instability that causes greater off-load axis, or an asymmetric separation. Schlieren images of the flow, as presented in Figure 10 also confirm a heavily asymmetric flow before transition, and RSS inception at NPR = 24.2.

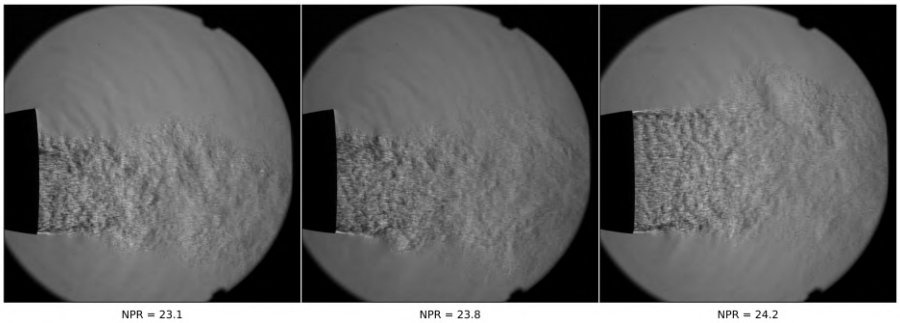

Figure 10: Compliant nozzle: Schlieren images depicting FSS → RSS transition occurring

Predominance of ovalisation is also in line with the findings of the GVT campaign, which revealed the ovalisation mode to be the fundamental natural oscillating frequency. One-sided power spectral densities G_{uu}(f) of each mode coefficient during steady-state operations at NPR = 22.3 were obtained and show a series of highly energetic narrowbands, as presented in Figure 11. The fact that these develop quite close to the natural frequencies of the static nozzle, as found in Table 2, lends support to a possible link with the natural oscillation modes of the nozzle. In this case, the presence

DOI: 10.13009/EUCASS2023-308

of an aerodynamic torque makes the coupled aeroelastic system *stiffer* than its static counterpart, thereby revealing a pre-stressed structure, which requires a higher driving frequency to resonate. Finally, even though each mode resonates at a stiffer eigenfrequency, they are also fully coupled with the fundamental frequency of ovalisation at 180 Hz.

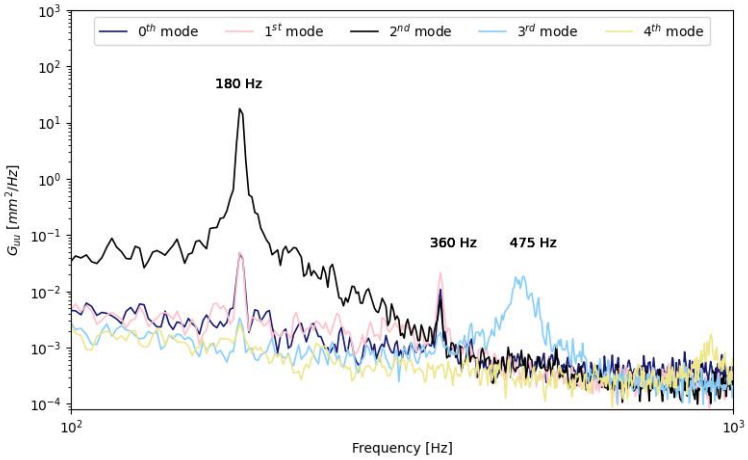

Figure 11: Power Spectral Density of the lip tracers modal coefficients for NPR = 22.3

3.2 Time-frequency analysis of the acoustic pressure waveforms

In order to extract spectral content from the acoustic pressure waveforms which result from transient test runs, a joint time-frequency analysis was carried out, by means of a wavelet analysis. Having proved itself as a powerful approach when analysing similar data to the one of the current research [19, 20], an analogous methodology, based on the implementation outlined by Torrence and Compo [32], was applied. The Morlet wavelet was chosen:

$$\psi(t/l) = e^{j\omega_\psi t/l} e^{-|t/l|^2/2} \tag{3}$$

with $|\omega_\psi = 6|$. The continuous wavelet transform of a discrete signal x_n consists in convolving the signal with a scaled and translated version of ψ. This process yields the wavelet coefficients, $\tilde{x}(l,t)$ following:

$$\tilde{x}(l,t) = \int x(t')\,\bar{\psi}\left(\frac{t'-t}{l}\right)dt, \tag{4}$$

where $\bar{\psi}$ indicates the wavelet complex conjugate. By varying the wavelet scale l it is possible to obtain a spectrogram illustrating both the amplitude of any feature with respect to the scale and how these amplitudes vary in time. In the current work, a range of frequencies comprised between 10 Hz and the Nyquist frequency $f_s/2$ = 25.6 kHz was resolved, employing a base-2 logarithmic set of 89 scales. Next, the Wavelet Power Spectrum (WPS) was obtained as:

$$E(l,t) = \frac{|\tilde{x}(l,t)|^2}{l} \tag{5}$$

Finally, the wavelet scale is converted to the equivalent Fourier frequency: $E(l,t) \rightarrow E(f,t)$, and, in the specific case of microphone signals, the spectra are presented in dB levels (ref: $20\,\mu Pa/\sqrt{Hz}$).

Figure 12 and Figure 13 present the results of the joint time-frequency space decomposition of the non-stationary acoustic pressure waveforms detected at $\phi = 69°$ for the stiff and compliant nozzle, respectively. At a first glance it can be seen that many phenomena involved in sound production are not easily predictable: this is proven by a mismatch between the acoustic spectrum and the constant Strouhal number curve plotted on the spectrograms. There is no indication that the signature scales to a constant Strouhal number, as is the case with most subsonic and perfectly expanded supersonic flows. At the bottom of each spectrogram, the raw signal and OASPL levels are also displayed. As far as the OASPLs are concerned, for the stiff nozzle, drops in the acoustic energy occur between NPR 11 and 15 and at NPR $\approx$ 25. In particular, $\text{OASPL}_{max} \approx$ 133 dB is registered at NPR = 11.3; then, acoustic energy gradually drops by 5 dB until NPR = 15, and rises again by 2 dB until NPR = 25. Finally, at transition, it sharply drops again by 3 dB. On the contrary, when considering the compliant nozzle noise emissions, sound pressure levels differ quite substantially,

DOI: 10.13009/EUCASS2023-308

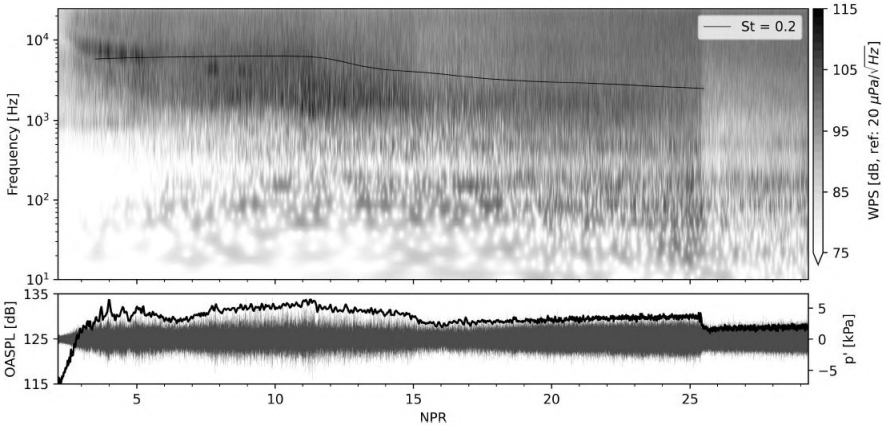

Figure 12: **Rigid nozzle startup** - Morlet wavelet power spectrum of the acoustic pressure measured at $\phi = 69°$ and expressed as $10\log_{10}(E(f,t)/ref^2)$ [dB, ref: 20 $\mu Pa/\sqrt{Hz}$]. Raw pressure signal (grey) is displayed at the bottom [kPa] with a moving window-averaged OASPL (black) [dB, ref: 20 μPa]

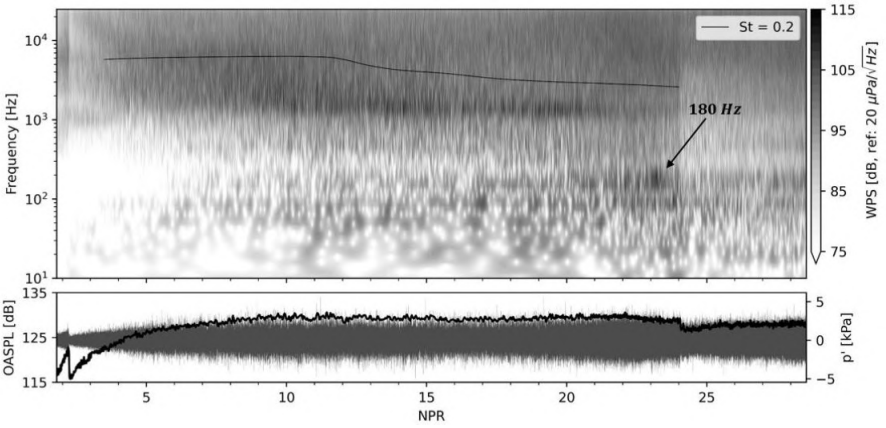

Figure 13: **Compliant nozzle startup** - Morlet wavelet power spectrum of the acoustic pressure measured at $\phi = 69°$ and expressed as $10\log_{10}(E(f,t)/ref^2)$ [dB, ref: 20 $\mu Pa/\sqrt{Hz}$]. Raw pressure signal (grey) is displayed at the bottom [kPa] with a moving window-averaged OASPL (black) [dB, ref: 20 μPa]

with the OASPL_{max} of the stiff nozzle being 3.5 dB higher in its period of maximum noise intensity around NPR = 11. Apart from a swift drop at transition, sound pressure levels remain quite steady throughout the whole FSS interval, at approximately the same levels that the stiff nozzle has between NPR = 15 and NPR = 23, during which the turbulent mixing noise dominates. This already gives an indication that, for the compliant nozzle, acoustic energy is attenuated at the higher frequencies and the dominant generation mechanism is turbulent mixing noise [33].

These claims are confirmed from the WPS topography. The rigid nozzle signature displays a few discernible features that can be linked to the unsteady flow behaviour. Flow transition is clearly visible at NPR = 25.7, and features a sudden drop of acoustic energy at all frequencies. Discrepancy from wall pressure measurements could be due to a partial transition in the bottom part of the nozzle around NPR = 24.5: the flow stays attached for a very short amount of time, before separating again. It could, therefore, be determined that said flapping motion, which is also at the core of side load generation, has induced an erroneous reading by the pressure sensors, due to the flow not being axisymmetric. Compliant nozzle's transition is also recognisable by a sudden drop of acoustic energy throughout the whole frequency range at approximately NPR = 24.4, thereby confirming that it occurs earlier in a similar way to what was also experimentally observed by Tinney et al. [22].

As far as noise mechanisms are concerned, the spectral trends in Figure 12 feature a high frequency band centred around 6.6 kHz, and extending between f = 5.5 kHz and f = 9 kHz. This fringe is comprised between NPR = 3 and NPR = 5.5 and has a smooth decreasing trend as the NPR increases. This behaviour, owing, most likely, to a broadening of the shock spacing, supports the hypothesis that these tones are associated with BBSN, as also documented by Donald et

DOI: 10.13009/EUCASS2023-308

al. [19] and Canchero et al. [34] at comparable NPRs. On the other hand, wall compliancy appears to be suppressing shock-associated noise: in the spectrum, there seems to be no evidence of BBSN at high frequencies. This feature has also been reported by Rojo et al. [20] when analysing the WPS of full-scale engines. Further proof of the possible presence or lack of BBSN tones is revealed through Fourier decomposition of the acoustic signal in azimuth. For this, data gathered when employing the circular microphone array is analysed based on a similar theoretical framework used for structural modal decomposition. BBSN is typically revealed by a dominant contribution of the 1^{st} azimuthal mode [35] and, as the results presented in Figure 14 show, for the stiff nozzle the asymmetric mode peaks at low NPRs, whereas it is suppressed in the signature of the flexible nozzle.

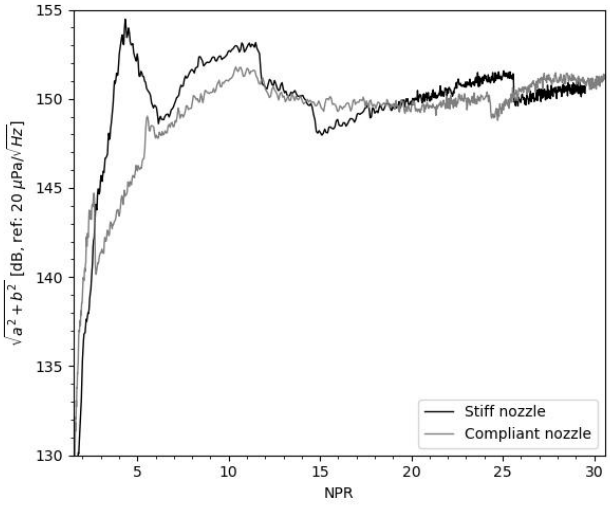

Figure 14: Comparison between stiff and compliant nozzle activity of the 1^{st} acoustic mode during startup operations, expressed as a moving window-averaged OASPL

3.3 Aeroelasticity effects on vibroacoustic loading

Despite most of the variance of the acoustic pressure signal is contained in the higher frequencies, a noticeable peculiarity of the acoustic spectrum presented in Figure 13 is an energetic peak centred around $f = 180$ Hz. This is also illustrated in Figure 15 which compares the acoustic performance of stiff and compliant nozzle while also reporting the energy spectra during operations of the compliant nozzle at lower fixed NPRs (11.3 and 18.9, repsectively). From the graph, it can be seen how the energetic peak around $f = 180$ Hz only becomes relevant before RSS transition in the compliant nozzle, and is not present in the spectra at the lower NPRs. The results of the modal analysis presented in Figure 11, together with the absence of the peak during operations of the stiff nozzle, or at lower NPR conditions of the compliant nozzle clearly suggest a link with structural vibrations.

A useful indicator that can be employed to better assess the coupling between an input x and an output signal y of a coupled system is *coherence*, denoted with γ^2_{xy}, which quantifies the degree of coupled energy as:

$$\gamma^2_{xy}(f) = \frac{\left|G_{xy}(f)\right|^2}{G_{xx}(f)G_{yy}(f)}$$

where G_{xy} is the cross-spectral density between x and y, and G_{xx} and G_{yy} are the auto-spectra of x and y, respectively. Based on this definition, and referring to the naming convention of Figure 7, coherence is computed between each of the detected raw microphone signals p' and their neighboring marker's fluctuation ρ'. The results presented in Figure 16 confirm a strong transfer of energy from the vibrating walls to the acoustic field around 180 Hz.
A possible explanation for this behaviour can be given considering the shock foot unsteadiness and its effects on the turbulent shear layer that is formed aft of the separation shock: the source of the aeroelastic tone detected by the microphones originates in the shear layer and is the result of the periodically amplified or dampened turbulent fluctuations that occur in response of the shock foot unsteadiness.

DOI: 10.13009/EUCASS2023-308

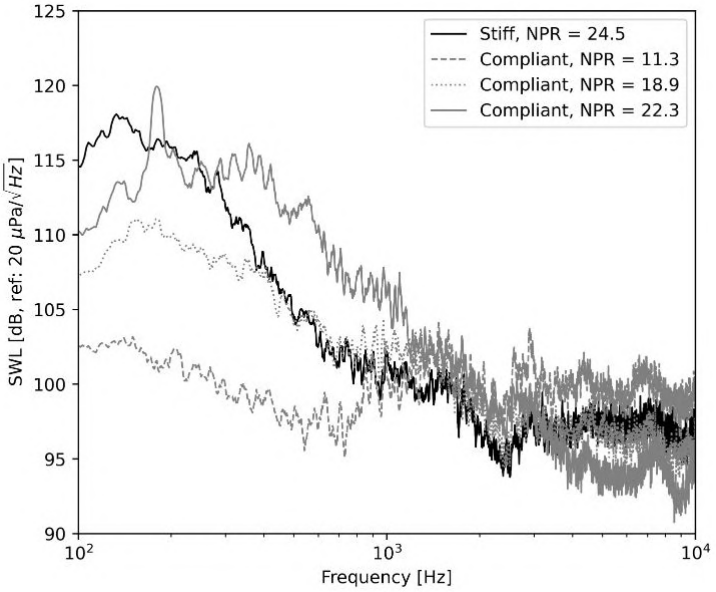

Figure 15: Comparison between stiff and compliant nozzle's one-sided PSD of the acoustic pressure waveforms detected from the South microphone, during steady state operations

4. Conclusions

A sub-scale nozzle testing facility was built in the Department of Flow Physics & Technology of the Faculty of Aerospace Engineering at Delft University of Technology to study fluid-structure interaction phenomena on TOP contoured nozzles during overexpanded operations.

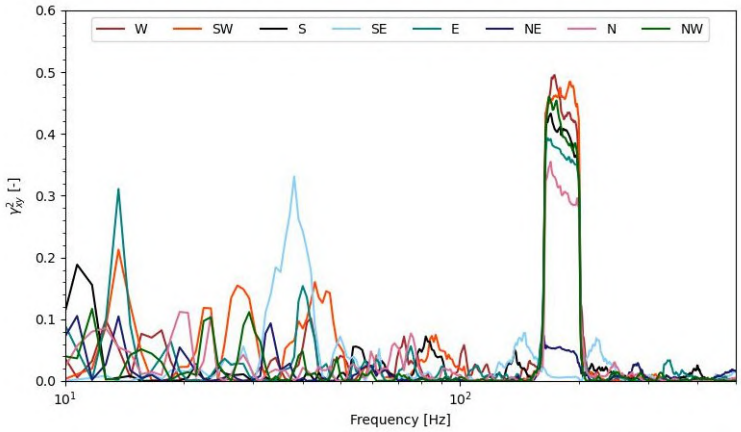

Figure 16: Linear coherence spectrum between acoustic pressure and marker displacement at 8 different locations at NPR = 22.3

Specifically, this work is part of a research effort to overcome the shortcomings associated with the current state-of-the art on rocket jet noise prediction. Experimental studies are still needed nowadays to investigate the acoustic signature of TOP contoured nozzles to identify the most relevant phenomena involved in the propagation of noise that is generated under a broad spectrum of mechanisms. This is especially necessary during the ignition transient: nevertheless, the main limitation of the currently available literature on the topic revolves around the fact that only stiff walled nozzles in which structural vibrations are suppressed have been employed. The goal of this study has been to provide a preliminary understanding on the effects that aeroelasticity has in noise generation during startup operations of compliant walled nozzles. Tests were conducted under comparable flow conditions and test parameters were measured by means of acoustic and optical techniques. Simultaneous recordings were performed and include the nozzle-wall deformation, by means of stereoscopic tracking of tracers on the nozzle lip, the imprint of the near-field acoustic signature, by means of

DOI: 10.13009/EUCASS2023-308

arrays of pressure-microphones, and Schlieren imaging of the jet plume. Comparison of results between the two test articles highlights a different spectral content and directivity pattern. Correlation between the structural displacements and the acoustic signal quantitatively aids the investigation of how fluid-structure interactions have an impact on the generation of an *aeroelastic tone* at 180 Hz. Findings suggest that its production could be the result of the periodic thickening and thinning of the shear layer owing to the heightened flapping motion of the nozzle lip preceding RSS transition, driven by an intensified shock foot instability.

5. Acknowledgements

We would like to give special thanks to Krijn de Kievit and Oliver F. Pearse, who worked extensively on the experimental test rig and nozzle testing capability prior to the execution of this work. We would also like to thank Dennis Bruikman, Peter Duyndam and Frits Donker Duyvis for their technical assistance. The authors also wish to acknowledge Victor Horbowiec for his support during the nozzle manufacturing phases and Jurij Sodja for his contribution during the ground vibration test campaign. Finally, we wish to gratefully acknowledge the Department of Flow Physics & Technology of the Faculty of Aerospace Engineering at Delft University of Technology for the financial support in establishing the experimental setup.

References

[1] G. V. R. Rao, "Exhaust Nozzle Contour for Optimum Thrust," *Journal of Jet Propulsion*, vol. 28, no. 6, pp. 377–382, 1958.

[2] W. J. Baars, C. E. Tinney, J. H. Ruf, A. M. Brown, and D. M. McDaniels, "Wall Pressure Unsteadiness and Side Loads in Overexpanded Rocket Nozzles," *AIAA Journal*, vol. 50, no. 1, pp. 61–73, 2012.

[3] M. Frey and G. Hagemann, "Flow separation and side-loads in rocket nozzles," in *35th Joint Propulsion Conference and Exhibit*, AIAA, 1999.

[4] L. Nave and G. Coffey, "Sea level side loads in high-area-ratio rocket engines," in *9th Propulsion Conference*, AIAA, 1973.

[5] H. Himelblau, D. Kern, L., and J. E. Manning, "NASA Handbook 7005 - Dynamics Environmental Criteria," tech. rep., NASA, 2001.

[6] C. K. W. Tam and K. C. Chen, "A statistical model of turbulence in two-dimensional mixing layers," *Journal of Fluid Mechanics*, vol. 92, no. 2, pp. 303–326, 1979.

[7] S. H. Oertel, "Mach wave radiation of hot supersonic jets investigated by means of a shock tube and new optical techniques," in *12th International Symposium on Shock-Tubes and Waves*, 1980.

[8] C. K. W. Tam and H. K. Tanna, "Shock associated noise of supersonic jets from convergent-divergent nozzles," *Journal of Sound and Vibration*, vol. 81, no. 3, pp. 337–358, 1982.

[9] J. L. Ellzey, M. R. Henneke, J. M. Picone, and E. S. Oran, "The interaction of a shock with a vortex: Shock distortion and the production of acoustic waves," *Physics of Fluids*, vol. 7, no. 1, pp. 172–184, 1995.

[10] K. B. M. Q. Zaman, M. D. Dahl, T. J. Bencic, and C. Y. Loh, "Investigation of a transonic resonance with convergent divergent nozzles," *Journal of Fluid Mechanics*, vol. 463, pp. 313–343, 2002.

[11] G. Raman, "Advances in Understanding Supersonic Jet Screech: Review and Perspective," *Progress in Aerospace Sciences*, vol. 34, no. 1, pp. 45–106, 1998.

[12] J. Onoda and K. Minesugi, "Estimation of mechanical environment of m-v satellite launcher," in *JSASS/JSME Structures Conference*, pp. 229–232, 1997.

[13] B. Henderson, C. Gerhart, E. Jensen, S. Griffin, and A. Lazzaro, "Vibroacoustic launch protection experiment," in *29th International Congress and Exhibition on Noise Control Engineering*, vol. 144(4), p. 2384, 2003.

[14] S. Griffin, S. Lane, and D. Leo, "Innovative vibroacoustic control approaches in space launch vehicles," in *29th International Congress and Exhibition on Noise Control Engineering*, 2000.

DOI: 10.13009/EUCASS2023-308

[15] K. M. Eldred, "Acoustic loads generated by the propulsion system," Tech. Rep. SP-8072, NASA Langley Research Center, 1971.

[16] S. A. McInerny and S. M. Ölçmen, "High-intensity rocket noise: Nonlinear propagation, atmospheric absorption, and characterization," *The Journal of the Acoustical Society of America*, vol. 117, no. 2, pp. 578–591, 2005.

[17] K. Plotkin, L. Sutherland, and B. Vu, "Lift-Off Acoustics Predictions for the Ares I Launch Pad," in *15th AIAA/CEAS Aeroacoustics Conference*, AIAA, 2009.

[18] J. Kenny, C. Hobbs, K. Plotkin, and D. Pilkey, "Measurement and Characterization of Space Shuttle Solid Rocket Motor Plume Acoustics," in *15th AIAA/CEAS Aeroacoustics Conference*, AIAA, 2009.

[19] B. Donald, W. Baars, C. Tinney, and J. Ruf, "Acoustic characterization of sub-scale rocket nozzles," in *50th AIAA Sciences Meeting*, AIAA, 2012.

[20] R. Rojo, C. E. Tinney, and J. H. Ruf, "Effect of Stagger on the Vibroacoustic Loads from Clustered Rockets," *AIAA Journal*, vol. 54, pp. 3588–3597, Nov. 2016.

[21] A. Canchero, C. E. Tinney, N. Murray, and J. H. Ruf, "Acoustic Imaging of Clustered Rocket Nozzles Undergoing End Effects," *AIAA Journal*, vol. 54, no. 12, pp. 3778–3786, 2016. Publisher: American Institute of Aeronautics and Astronautics.

[22] C. E. Tinney, K. Scott, M. Routon, J. Sirohi, and J. Ruf, "Effect of Aeroelasticity on Vibroacoustic Loads during Startup of Large Area Ratio Nozzles," in *23rd AIAA/CEAS Aeroacoustics Conference*, AIAA, 2017.

[23] K. De Kievit, "Development of a rocket nozzle test facility for measurements of fluid-structure interaction phenomena," Master's thesis, Delft University of Technology, 2021.

[24] J. Ruf, D. McDaniels, and A. Brown, "Nozzle Side Load Testing and Analysis at MSFC," in *45th Joint Propulsion Conference & Exhibit*, AIAA, 2009.

[25] G. R. Nickerson, L. D. Dang, and D. E. Coats, "Engineering and programming manual: Two-dimensional kinetic reference computer program (TDK)," Tech. Rep. SN-63, 1985.

[26] T.-S. Wang, X. Zhao, S. Zhang, and Y.-S. Chen, "Development of an Aeroelastic Modeling Capability for Transient Nozzle Flow Analysis," *Journal of Propulsion and Power*, vol. 30, no. 6, pp. 1692–1700, 2014.

[27] C. Génin, R. Stark, and S. Jack, "Flow separation in out-of-round nozzles, a numerical and experimental study," in *Progress in Flight Physics*, vol. 7, pp. 269–282, 2015.

[28] D. R. Chapman, D. M. Kuehn, and H. K. Larson, "Investigation of Separated Flows in Supersonic and Subsonic Streams with Emphasis on the Effect of Transition," 1958.

[29] P. Carriere, M. Seriexix, and J. L. Solignac, "Properties de Similitude des Phenomenes de Decollement Laminaires ou Turbulents en Ecoulement Supersonic Nonuniforme," in *Proceedings of the 12th International Congress of Applied Mechanics*, pp. 145–157, 1968.

[30] R. Stark and B. Wagner, "Experimental study of boundary layer separation in truncated ideal contour nozzles," *Shock Waves*, vol. 19, no. 3, pp. 185–191, 2009.

[31] B. Wieneke, "Iterative reconstruction of volumetric particle distribution," *Meas. Sci. Technol.*, vol. 24, no. 2, 2012.

[32] C. Torrence and G. Compo, "A practical guide to wavelet analysis," *Bulletin of the American Meteorological Society*, vol. 79, no. 1, pp. 64–78, 1998.

[33] C. K. W. Tam, K. Viswanathan, K. K. Ahuja, and J. Panda, "The sources of jet noise: experimental evidence," *Journal of Fluid Mechanics*, vol. 615, pp. 253–292, Nov. 2008. Publisher: Cambridge University Press.

[34] A. Canchero, C. E. Tinney, N. Murray, and J. H. Ruf, "Flow and Acoustics of Clustered Rockets During Startup," *AIAA Journal*, vol. 54, no. 5, pp. 1660–1669, 2016.

[35] M. H. Wong, R. Kirby, P. Jordan, and D. Edgington-Mitchell, "Azimuthal decomposition of the radiated noise from supersonic shock-containing jets," *The Journal of the Acoustical Society of America*, vol. 148, no. 4, pp. 2015–2027, 2020.